Lawrence Berkeley National Laboratory

Title
Effect of (1 1 1)-oriented strain on the structure and magnetic properties of La0.7Sr0.3MnO3 thin films

Permalink
https://escholarship.org/uc/item/1256q840

Journal
Journal of Physics Condensed Matter, 30(25)

ISSN
0953-8984

Authors
Bolstad, T
Lysne, E
Hallsteinsen, I
et al.

Publication Date
2018-06-27

DOI
10.1088/1361-648x/aac468

Peer reviewed

PAPER

Effect of (1 1 1)-oriented strain on the structure and magnetic properties of La$_{0.7}$Sr$_{0.3}$MnO$_3$ thin films

To cite this article: T Bolstad *et al* 2018 *J. Phys.: Condens. Matter* **30** 255702

View the article online for updates and enhancements.

IOP | ebooks™

Bringing you innovative digital publishing with leading voices to create your essential collection of books in STEM research.

Start exploring the collection - download the first chapter of every title for free.

Effect of (1 1 1)-oriented strain on the structure and magnetic properties of La$_{0.7}$Sr$_{0.3}$MnO$_3$ thin films

T Bolstad[1], E Lysne[1], I Hallsteinsen[1,2], E Arenholz[2], U L Österberg[1] and T Tybell[1]

[1] Department of Electronic Systems, NTNU Norwegian University of Science and Technology, 7491 Trondheim, Norway
[2] Advanced Light Source, Lawrence Berkeley National Laboratory, Berkeley, CA 94720, United States of America

E-mail: thomas.tybell@ntnu.no

Abstract
Using strain, i.e. subtle changes in lattice constant in a thin film induced by the underlying substrate, opens up intriguing new ways to control material properties. We present a study of the effects of strain on structural and ferromagnetic properties of (1 1 1)$_{pc}$-oriented La$_{0.7}$Sr$_{0.3}$MnO$_3$ epitaxial thin films grown on NdGaO$_3$, SrTiO$_3$, and DyScO$_3$ substrates. (The subscript pc denotes the pseudo-cubic symmetry.) The results show that La$_{0.7}$Sr$_{0.3}$MnO$_3$ assumes a monoclinic unit cell on NdGaO$_3$ and DyScO$_3$ and a rhombohedral unit cell on SrTiO$_3$. For La$_{0.7}$Sr$_{0.3}$MnO$_3$ on NdGaO$_3$ and DyScO$_3$ a uniaxial magnetic anisotropy is found, while La$_{0.7}$Sr$_{0.3}$MnO$_3$ on SrTiO$_3$ is magnetically isotropic. The Néel model is used to explain the anisotropy of the thin films on NdGaO$_3$ and SrTiO$_3$, however, for La$_{0.7}$Sr$_{0.3}$MnO$_3$ on DyScO$_3$ the effect of octahedral rotations needs to be included through the single ion model. Through examination of the Curie temperature of the strained films we suggest that (1 1 1)-strain has a different effect on the Jahn–Teller splitting of e_g and t_{2g} electron levels than what is seen in (0 0 1)$_{pc}$-oriented La$_{0.7}$Sr$_{0.3}$MnO$_3$ thin films.

Keywords: strain, LSMO, magnetic anisotropy, crystal symmetry

S Supplementary material for this article is available online

(Some figures may appear in colour only in the online journal)

Introduction

Control of magnetic properties is important for the realization of spintronic devices such as magnetic tunnel junctions. Central to the realization of such devices is the possibility to tune the magnetic anisotropy [1]. Epitaxial thin film synthesis allows tuning the magnetic properties by inducing tensile or compressive strain in thin films through suitable choice of substrate. Especially, the magnetic anisotropy has been shown to be susceptible to both strain and symmetry, controllable in thin films through the choice of substrate [2–6]. Connected to strain engineering is understanding the effect of octahedral rotations on thin film properties. Oxygen octahedral rotations

are responsible for a thickness driven change in anisotropy direction for La$_{0.7}$Sr$_{0.3}$MnO$_3$ (LSMO) films on (0 0 1)$_{pc}$-oriented substrates [7] (We use the subscripts c, pc, rh, h, o, m, and t for cubic, pseudocubic, rhombohedral, hexagonal, orthorhombic, monoclinic and triclinic, respectively.). In LSMO/Eu$_{0.7}$Sr$_{0.3}$MnO$_3$ superlattices the creation of octahedral superstructures enables spatial control of the ferromagnetism and electronic bandwidth [8].

An intriguing material to study in this regard is LSMO, a room temperature ferromagnetic perovskite oxide with a near 100% spin-polarization, and a strong coupling between atomic structure on the one hand and electronic and magnetic properties on the other hand [9, 10]. In bulk, LSMO is

twinned rhombohedral and reported to have either an $(111)_{pc}$ easy plane of magnetization [11, 12], or $(111)_{pc}$ easy direction [13]. Extensive research has focused on tuning the magnetic anisotropy by strain in thin films with a $(001)_{pc}$ surface orientation [12]. For thin films of LSMO on cubic substrates, tetragonal and monoclinic unit cell structures have been reported under tensile strain on $(001)_c$-oriented $SrTiO_3$ (STO), while under compressive strain on $(001)_c$-oriented $(LaAlO_3)_{0.3}$-$(Sr_2AlTaO_6)_{0.7}$ (LSAT) only monoclinic unit cell structures are reported [14, 15]. In both cases a biaxial anisotropy with magnetically easy axes along the $\langle 110 \rangle_{pc}$ directions are reported, with an additional uniaxial contribution in the case of LSAT [2, 6]. For orthorhombic substrates a monoclinic structure is found for both LSMO under tensile strain on $(110)_o$-oriented $DyScO_3$ (DSO) and under compressive strain on $(001)_{pc}$-oriented $NdGaO_3$ (NGO) [15]. The anisotropy of tensile strained LSMO on orthorhombic substrates is uniaxial, with the easy axis aligned along the direction of the largest strain, except for $(11-2)_o$ oriented NGO where the easy axis has been reported to change with film thickness [4, 5, 16]. In addition to tuning the magnetic properties with strain, changing the crystallographic orientation opens further avenues for property engineering. For LSMO on STO it has been found that the interfaces of $(110)_c$ and $(111)_c$-oriented LSMO are more bulk-like as a function of thickness than $(001)_c$-oriented interfaces [17], while differences in switching mechanisms and anisotropy are observed between films of LSMO on $(001)_o$ and $(100)_o$-oriented NGO [18].

Recently, the interest in $(111)_{pc}$-oriented films has grown considerably due to the possibilities offered by symmetry engineering on such facets by strain. The three-fold symmetry has been shown to result in emerging properties like polar metals [19], exchange bias at the interface between a ferromagnetic and a paramagnetic material [20], switchable ferrimagnetic moments as result of interface oxygen octahedral rotations [21], and predicted Goldstone-like behavior of compressively strained $LaAlO_3$ (LAO) [22]. The magnetic anisotropy of LSMO on $(111)_c$-oriented STO has been found to have a weak in-plane anisotropy following the high symmetry directions of the substrate [23], different from when deposited on (001)-oriented STO.

In order to address how (111)-strain affects the structural symmetry and magnetic anisotropy of LSMO thin films we synthesized LSMO thin film on a range of different substrates and determined material properties using x-ray diffraction and magnetic characterization techniques. The results point towards a distinct response to strain as compared to (001)-strain, and the possibility to employ strain in (111)-oriented thin films to tailor the magnetic anisotropy of LMSO.

Experimental

Epitaxial LSMO films of 19 nm to 26 nm thickness were grown on $(011)_o$-oriented NGO, $(111)_c$-oriented STO, and $(101)_o$-oriented $DyScO_3$ (DSO) substrates (all corresponding to $(111)_{pc}$ facets) by pulsed laser deposition. The STO
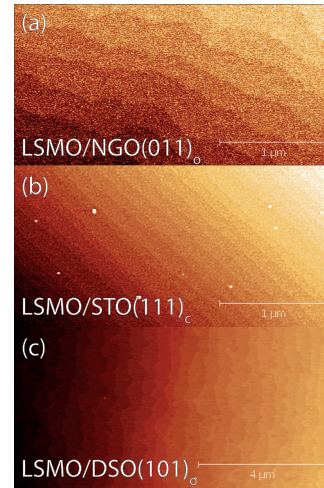
Figure 1. AFM micrographs of the surfaces of LSMO grown on (a) $(011)_o$-oriented NGO, (b) $(111)_c$-oriented STO, and (c) $(101)_o$-oriented DSO.

substrates were prepared by etching in buffered hydrofluoric acid for 45 s following annealing at 1050 °C in oxygen flow. The NGO and DSO substrates was annealed for two hours at 1000 °C in oxygen flow. A KrF excimer laser ($\lambda = 248$ nm) with a fluence of ~2 J cm^{-2} and a repetition rate of 1 Hz was employed to ablate material from a stoichiometric LSMO target. The substrates were heated to 540 °C in a 0.35 mbar oxygen atmosphere during deposition with a target to substrate distance of 45 mm, in order to ensure 2D growth [24]. During deposition, the growth was monitored with reflection high-energy electron diffraction (RHEED). The samples were cooled in a 100 mbar oxygen atmosphere after deposition. After deposition the film topography was characterized with atomic force microscopy (AFM, Veeco Nanoscope V). Micrographs of the surfaces of the films grown on NGO, STO and DSO are shown in figures 1(a)–(c), respectively, with well-defined steps and terraces, indicating high film quality.

Bulk LSMO has a rhombohedral unit cell (space group R-3c) with $a_r = 5.471$ Å and $\alpha_r = 60.43°$ [25]. Both NGO and DSO have an orthorhombic unit cell (space group Pbnm) with lattice parameters $a_o = 5.427$ Å, $b_o = 5.500$ Å, $c_o = 7.705$ Å [26], and $a_o = 5.44$ Å, $b_o = 5.71$ Å, $c_o = 7.89$ Å [27], respectively. STO is cubic (space group Pm-3m) with lattice constant $a = 3.905$ Å [28]. The strain along an $[hkl]$ direction is defined as $\varepsilon_{hkl} = (d_{hkl,\text{sub}} - d_{hkl,\text{bulk}})/d_{hkl,\text{bulk}}$, with $d_{hkl,\text{sub}}$ and $d_{hkl,\text{bulk}}$ being the lattice parameter of the substrate and bulk LSMO, respectively. The calculated strain values along the primary in-plane directions ($[1-10]_{pc}$ and $[11-2]_{pc}$) can be found in table 1.

The crystalline structure of the LSMO thin films was characterized using a four-circle, high-resolution x-ray diffractometer (XRD, Bruker D8). Rocking curves around the LSMO $(111)_{pc}$ reflection reveal full width at half maximum values between 0.035° and 0.04°, on the same order as for the substrates, indicating high quality films. Reciprocal space maps were recorded around asymmetrical reflections. For the thin film on STO, the $(330)_c$, $(114)_c$, $(312)_c$ and $(132)_c$ reflections (in this work we use parenthesis to denote reflections

Table 1. In-plane lattice parameters and strain values for LSMO$(1\,1\,1)_{pc}$ on NGO$(0\,1\,1)_o$, STO$(1\,1\,1)_c$, and DSO$(1\,0\,1)_o$ substrates. The in-plane directions is in pseudocubic notation with $[1-1\,0]$ pseudocubic corresponding to $[2\,0\,0]$ and $[0\,2\,0]$ orthorhombic in-plane directions for NGO and DSO, respectively, and $[1\,1\,-2]$ pseudocubic corresponding to $[0\,2\,-4]$ and $[2\,0\,-4]$ orthorhombic. $\varepsilon_{avg} = (\varepsilon_{1-1\,0} + \varepsilon_{1\,1-2})/2$.

| Substrate	$d_{1-1\,0}$ (Å)	$d_{1\,1-2}$ (Å)	$\varepsilon_{1-1\,0}$ (%)	$\varepsilon_{1\,1-2}$ (%)	ε_{avg} (%)
NGO	2.72	1.58	−1.04	−0.35	−0.70
STO	2.76	1.59	0.64	0.64	0.64
DSO	2.86	1.60	4.06	0.81	2.44

to ease inclusion of crystal symmetry subscript) were used to determine the film's unit cell. The same reflections (corresponding to $(0\,2\,8)_o$, $(0\,6\,0)_o$, $(2\,4\,4)_o$ and $(-2\,4\,4)_o$) were used for the film on NGO. However, for the film deposited on DSO the $(2\,0\,8)_o$, $(6\,0\,0)_o$, $(3\,1\,6)_o$, and $(3\,-1\,6)_o$ reflections (corresponding to $(3\,3\,0)_{pc}$, $(1\,1\,4)_{pc}$, $(2\,3\,1)_{pc}$ and $(3\,2\,1)_{pc}$) were utilized, as substrate reflections overlap the film reflections for the $(4\,2\,4)_o$ and $(4\,-2\,4)_o$ peaks. In addition, the symmetrical $(1\,1\,1)_{pc}$ reflection was used for all structures.

Magnetic measurements were performed using a vibrating sample magnetometer (VSM). Due to a strong paramagnetic signal from both NGO and DSO substrates, hysteresis measurements were also performed by MOKE at room temperature. Magnetic anisotropy was investigated using the magneto-optical Kerr effect in the longitudinal configuration (L-MOKE) at room temperature. Hysteresis curves were measured at different angles by rotating the samples in a sinusoidal *H*-field (in the plane of the film). An alternating magnetic field with an amplitude of 100 Oe and a frequency of 10 Hz was used to achieve full saturation of the samples. Each hysteresis curve was calculated as average of 1000 individual loops.

To ensure that the observed MOKE signal does not originate from the NGO and DSO substrates, element specific x-ray magnetic circular dichroism (XMCD) spectroscopy at beamline 4.0.2 at the advanced light source (ALS) has been performed (see supplementary materials figures S1 and S2 available online at stacks.iop.org/JPhysCM/30/255702/mmedia).

Results and discussion

Figure 2 depicts θ-2θ scans of the $(1\,1\,1)_{pc}$ peaks for LSMO deposited on DSO, STO, and NGO respectively. The position of the $(1\,1\,1)_{pc}$ reflection of LSMO shifts due to strain from the substrates, the average strain being −0.70%, 0.64%, and 2.44% for NGO, STO, and DSO, respectively. In figures 3(a)–(c) reciprocal space maps (RSM) of LSMO on the three substrates are shown. For all films the in-plane component of the film peak is coinciding with the value of the substrate, confirming coherent film growth. The features $(Q_\perp)$ indicating the out of plane lattice constant in figure 3(a) for LSMO on STO does not depend on the choice of reflection. On $(0\,0\,1)$-oriented STO this would correspond to a tetragonal unit cell. However, due to the trigonal symmetry of the $(1\,1\,1)_{pc}$ STO surface, the
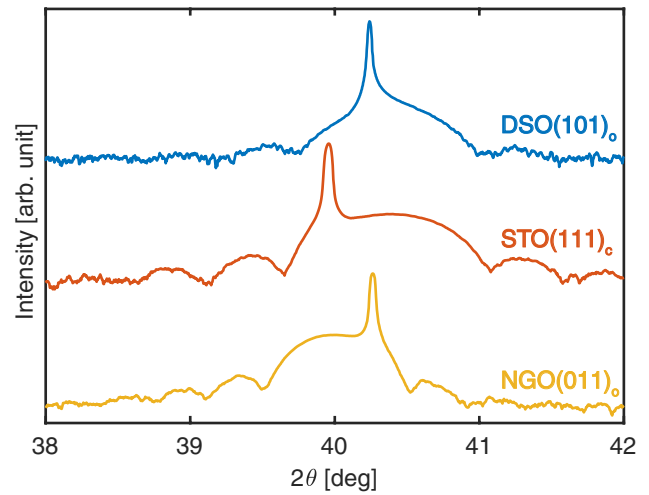

Figure 2. Linear $\theta/2\theta$ scans of the $(1\,1\,1)_{pc}$ peaks of LSMO on DSO, STO and NGO substrates.

constant $Q_\perp$ value indicates a rhombohedral/hexagonal unit cell. Similarly, the RSM data for LSMO on DSO reveal a constant value for the out-of-plane parameter for the reflections investigated (figure 3(b)). Due to the orthorhombic symmetry of the DSO substrate, this is consistent with a monoclinic unit cell of LSMO. We note that the data for LSMO on DSO also can be represented by a strained hexagonal unit cell. To establish a hexagonal unit cell on a $(1\,1\,1)_{pc}$-oriented surface the relation between the primary in-plane directions needs to be $1/\sqrt{3}$. This is not the case for an orthorhombic unit cell, though due to the out-of-plane symmetry found in the RSM data, a strained hexagonal unit cell can be inferred with $\gamma = 118.2°$, smaller than $\gamma = 120°$ in a proper hexagonal unit cell. Figure 3(c) shows the reflections for LSMO on NGO. Here the out-of-plane peak positions vary, revealing a triclinic unit cell. The refined unit cell parameters are listed in table 2, while figures 4(a)–(c) depicts the resulting unit cells and their relationship to the substrate. Here, LSMO under compressive strain (NGO) is found to be triclinic while it is monoclinic when deposited on $(0\,0\,1)_{pc}$-oriented NGO. However, it is possible to obtain a monoclinic unit cell for compressively strained $(1\,1\,1)_{pc}$ LSMO on NGO by tuning the laser-fluence during deposition (see supplementary materials, figure S3). The triclinic LSMO film on NGO presented here has been grown using the same laser-fluence as the rhombohedral and monoclinic films on STO and DSO, respectively.

The structure of rhombohedral LSMO can be expressed using a monoclinic unit cell, enabling a more detailed comparison between the different systems. In figure 4(d) the evolution of the lattice parameters and distortion angle as a function of average in-plane strain, $\varepsilon_{\|,avg} = (\varepsilon_{\|,1-1\,0_{pc}} + \varepsilon_{\|,1\,1-2_{pc}})/2$ is shown. The values for bulk unstrained LSMO are plotted as open circles. For all films, the *b*-parameter is chosen as the parameter locked to the substrate. This corresponds to the $[1\,0\,0]_o$ $[1-1\,0]_{,c}$, and $[0\,1\,0]_o$ directions for the NGO, STO and DSO substrates, respectively. All free parameters, a_m, c_m, β, vary to accommodate the strain.

The β angle increases from $\beta < 90°$ for compressive strain to $\beta > 90°$ for tensile strain ($\beta = 90.5°$ for bulk LSMO).
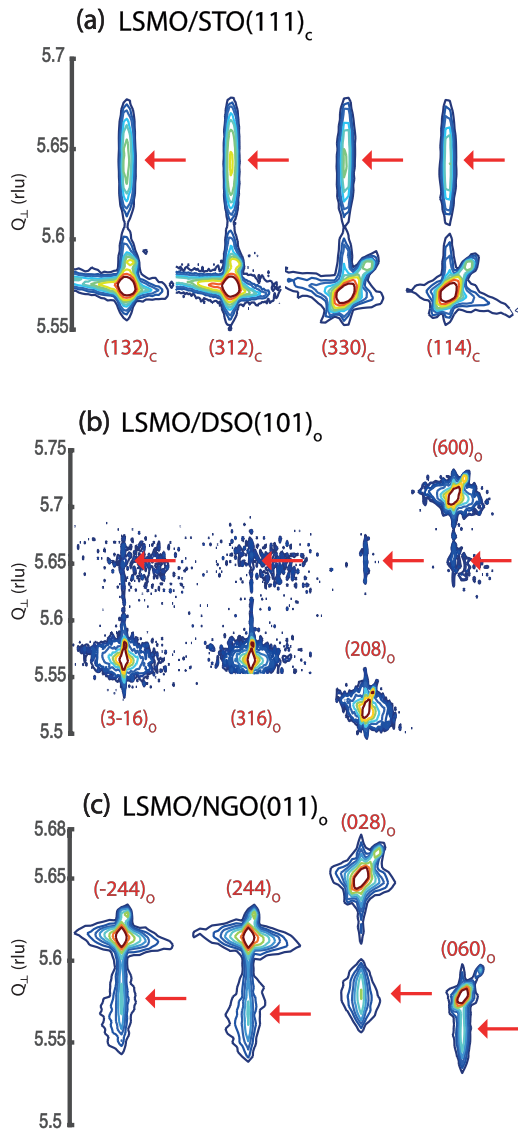
Figure 3. Reciprocal space maps of the LSMO films on (a) STO ((1 3 2)$_c$, (3 1 2)$_c$, (3 3 0)$_c$, and (1 1 4)$_c$ reflections), (b) DSO ((4 −2 4)$_o$, (4 2 4)$_o$, (2 0 8)$_o$, and (6 0 0)$_o$ reflections), (c) NGO ((−2 4 4)$_o$, (2 4 4)$_o$, (0 2 8)$_o$, and (0 6 0)$_o$ reflections). The out-of-plane reciprocal space vector is defined as $Q_\perp = 4\pi/\lambda\sin(\theta)$ with $\lambda = 1.540\,598$ Å.

Under tensile strain, only a change in β is found to accommodate the strain as c_m and a_m, are found to be constant between the films on STO and DSO. This is not the case moving in to the compressive regime, where all lattice parameters change as compared to the tensile strained films. In (0 0 1)$_{pc}$-oriented films the same trend is reported [15]. For both (0 0 1)$_{pc}$ and (1 1 1)$_{pc}$-oriented LSMO under tensile strain, this results in a twofold symmetry, and that tensile strained LSMO, regardless of orientation, has a higher symmetry as compared to compressive strained LSMO.

Figure 4(e) shows the unit cell volume and out of plane distortion, $\varepsilon_\perp$, versus average in-plane strain, $\varepsilon_{\parallel,avg}$. A close to linear relationship is found for the unit cell volume, with the unit cell volume increasing with increasing tensile strain. Both the behavior and magnitude matches

results found for (0 0 1)-oriented LSMO-films [15]. From the linear θ-2θ scans, see figure 2, the out of plane lattice spacing of the films can be found. From the average in-plane strain, $\varepsilon_{\parallel,avg}$, versus the out of plane distortion $\varepsilon_\perp$ ($\varepsilon_\perp = \varepsilon_{111_{pc}} = (d_{111_{pc},film} - d_{111_{pc},bulk})/d_{111_{pc},bulk}$) the effective Poissons ratios can then be calculated using $\nu = 1/(1 - 2\varepsilon_{\parallel,avg}/\varepsilon_\perp)$ [29]. The obtained Poissons ratio for LSMO on NGO and STO is 0.41, slightly larger than found for (0 0 1)-oriented LSMO films of 0.37 [30]. For LSMO on DSO a substantially lower Poissons ratio is found, 0.16, implying a non-linear response between in-plane strain and out-of-plane distortion for (1 1 1)-oriented LSMO films.

The film strain affects the magnetic properties of the thin films. The magnetization of (1 1 1) oriented LSMO on STO is macroscopically isotropic, as seen in figure 5(a). This is in full agreement with previously reported results [23] of a weak microscopic anisotropy with a six-fold symmetry, resulting in a macroscopically isotropic response. By utilizing the Néel model of magnetic anisotropy [31], which has been used to explain the magnetic anisotropy of (0 0 1)$_{pc}$ and (1 1 0)$_{pc}$-oriented LSMO thin films, an analytical expression for the anisotropy energy of a rhombohedral unit cell can been found [32]:

$$E = -6\delta L(r_0)\left(\cos^2(\theta) - \frac{1}{2}\right)$$

where the largest angle on each side face of the rhombohedral unit cell is modeled as $90^\circ + 2\delta$, $L(r_0)$ is the dipolar Néel parameter at the equilibrium value r_0, which for LSMO is found to be negative, and θ is the angle of the magnetization with the [1 1 1]$_c$ direction. This results in an easy (1 1 1)$_c$ plane, corroborating the experimental results. A surface plot of the anisotropy energy can be seen in the insert of figure 5(a).

Figures 5(b) and (c) show MOKE data for LSMO on NGO and DSO, respectively, exhibiting a strong in-plane anisotropy. LSMO on NGO shows a clear difference between the [1 0 0]$_o$ and [0 1 −1]$_o$ in-plane directions (figure 5(b)), with [1 0 0]$_o$ as magnetically hard axis with a close to linear response to the applied field, while the response to the applied magnetic field along the [0 1 −1]$_o$ easy axis leads to nearly square hysteresis curve. The Néel model predicts an easy axis along the most tensile strained direction, which in this case is [0 1 −1]$_o$. Solving the Néel model for a triclinic unit cell numerically (supplementary material figure S4) a two-fold magnetic anisotropy is found with easy axis and hard axis along [0 1 −1]$_o$ and [1 0 0]$_o$, respectively.

From the Néel model it is expected that LSMO films on DSO will have an easy axis along the direction of largest tensile strain, i.e. [0 1 0]$_o$. However, the data reveals a hard axis along the [0 1 0]$_o$ direction and an easy axis along [1 0 −1]$_o$ as shown in figure 5(c). Hence, applying the Néel model does not replicate the observed effective magnetic anisotropy (supplementary material figure S5). We note that the Néel model only considers bond length and angle between the Mn atoms. As the source of the magnetization in LSMO is the double exchange mechanism, the angle and length of the Mn–O–Mn bonds are important for the magnetic characteristics, and can be incorporated in a single ion model [33]. This model

**Table 2.** The refined unit cell parameters for LSMO films deposited on NGO(011)$_o$, STO(111)$_c$, and DSO(101)$_o$.

Substrate	Structure	a (Å)	b (Å)	c (Å)	α (°)	β (°)	γ (°)
NGO	Triclinic	5.51	5.43	7.75	90.1	89.5	90.1
STO	Rhombohedral	5.47					60.7
DSO	Monoclinic	5.47	5.73	7.78	90	90.9	90
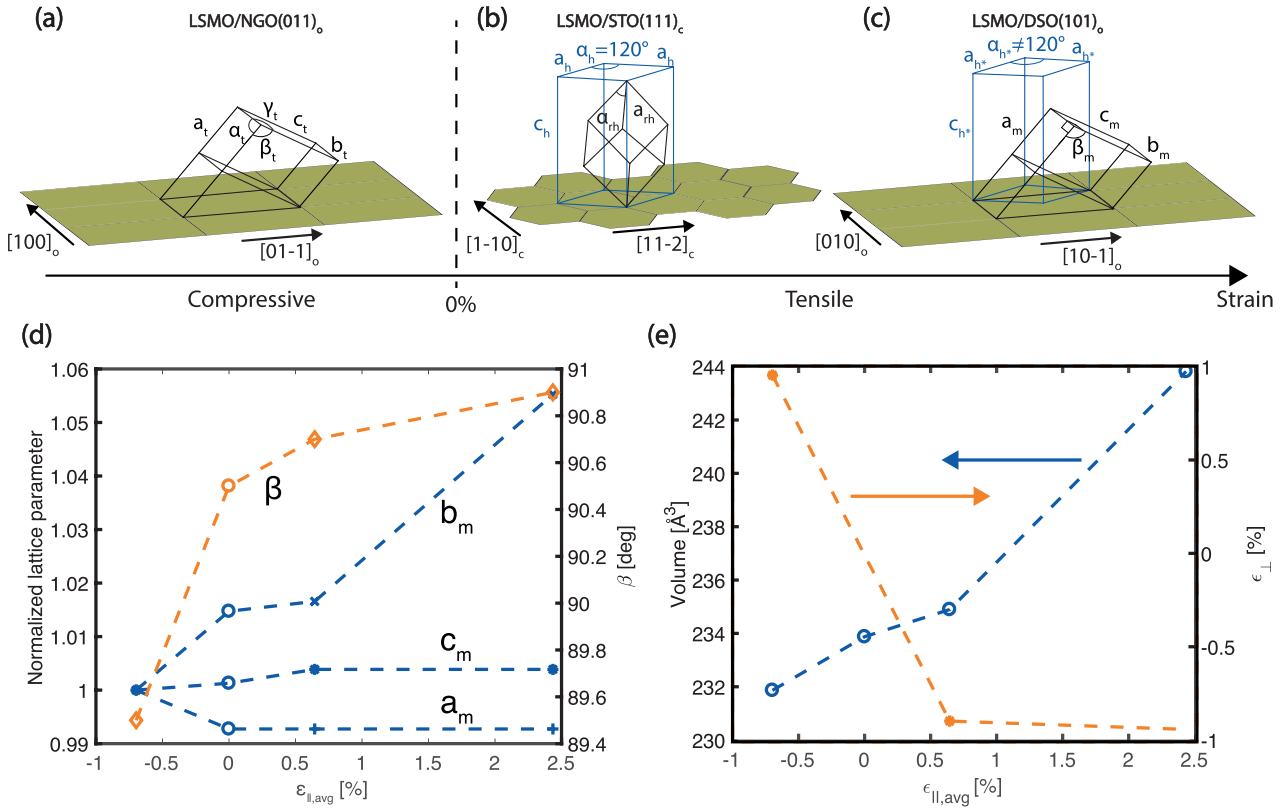
Figure 4. Sketches of the resulting unit cells obtained from the RSM data. (a) Triclinic (t) LSMO on (011)$_o$-oriented NGO. (b) Rhombohedral (rh, black) or hexagonal (h, blue) LSMO on (111)$_c$-oriented STO. (c) Monoclinic (m, black) or distorted hexagonal (h*, blue) LSMO on (101)$_o$-oriented DSO. (d) Normalized lattice parameters and angle α as a function of average in-plane strain. The unit cell volumes for bulk LSMO and LSMO on STO are found by expressing their rhombohedral unit cells as monoclinic. The values for bulk LSMO are shown as open circles. (e) Measured out-of-plane strain and volume versus average in-plane strain. Bulk values are marked at open circles.
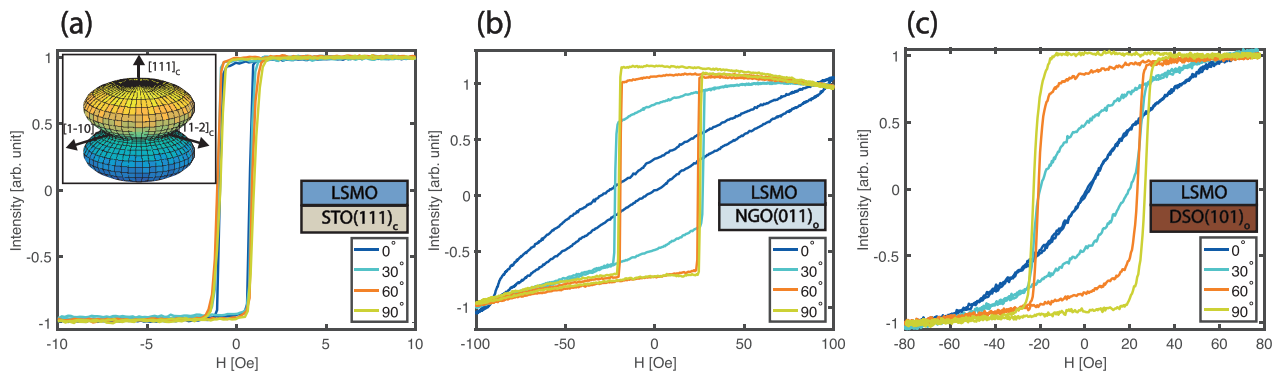
Figure 5. (a) Magnetization data for LSMO on STO. 0° corresponds to the [1−10]$_c$ direction. The insert shows a surface plot of the magnetic anisotropy energy of LSMO on STO. (b) Magnetization data for LSMO on NGO. 0° corresponds to the [100]$_o$ ([1 −10]$_{pc}$) direction. (c) Magnetization data for LSMO on DSO. 0° corresponds to the [0 10]$_o$ ([1 −10]$_{pc}$) direction.
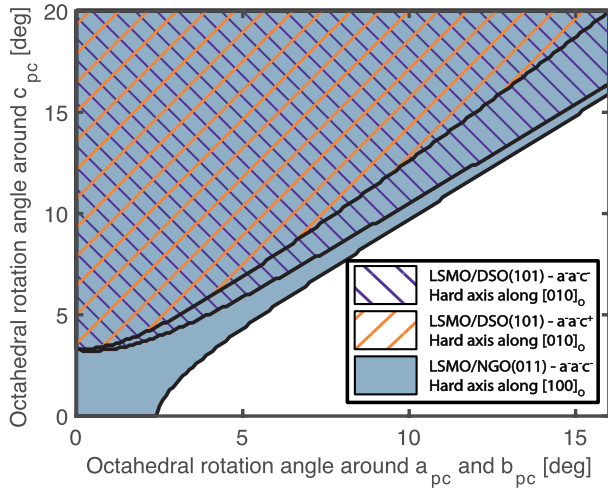
Figure 6. Octahedral rotation angle dependence of the hard axis direction for LSMO on DSO for $a^-a^-c^-$ and $a^-a^-c^+$ rotation patterns and LSMO on NGO for $a^-a^-c^-$ rotation pattern are calculated using the single ion model. The octahedral rotation combinations that result in an anisotropy matching the experimentally found anisotropy are shown as striped areas for the film on DSO and as shaded blue for the film on NGO.

Figure 7. Remanent magnetization of the LSMO films on NGO, STO and DSO for the temperature range around the Curie temperatures.

assumes that the crystal field is a sum of the atomic crystal fields and a strong spin–orbit coupling. The anisotropy energy from a single Mn–O bond is given by:

$$E_i = -\frac{eQQ_2}{16\pi\varepsilon_0 R_i^3}(3\cos^2\theta_i - 1)$$

where e is the electron charge, Q is the effective charge of the ligand, Q_2 is the quadrupole moment of the magnetic ion, ε_0 is the vacuum permittivity, R_i is the Mn–O bond length, and θ_i is the angle between the magnetization direction and the Mn–O bond. E_i is summed over all bonds in a two by two by two structure of pseudo-cubic unit cells to find the total anisotropy energy E. By applying the single ion model, without octahedral rotations, the same result as for the Neel model must be obtained. This results in QQ_2 being negative for LSMO on DSO and NGO.

Using the single ion model, the magnetic anisotropy of LSMO films on DSO and NGO can be expressed as a function of octahedral rotations. For LSMO on DSO the monoclinic unit cell can have three possible rotation patterns in the Glazer tilt system [34], $a^-b^-c^0$ (#12), $a^-a^-c^-$ (#15), or $a^-b^-c^+$ (#11). As the a_{pc} and b_{pc} are mirror symmetrical across the $(010)_o$ plane, the rotations need to be symmetrical across that plane and consequently $a^-a^-c^0$, $a^-a^-c^-$, or $a^-a^-c^+$ are possible. For LMSO on NGO the triclinic unit cell can only have the rotation system $a^-b^-c^-$ (#2). Since triclinic distortion in this case is small ($\alpha = 90.1°$, $\gamma = 90.1°$), the difference in rotation magnitudes around a_{pc} and b_{pc} will be small, and are therefore here treated as equal. The resulting anisotropy phase diagram can be seen in figure 6, with the shaded regions indicating the intervals of rotation magnitudes that recreate the observed anisotropy for LSMO on DSO and NGO.

With regards to LSMO on DSO, rotations of at least 3.3° around c_{pc} is needed, ruling out $a^-a^-c^0$ as a possible rotation
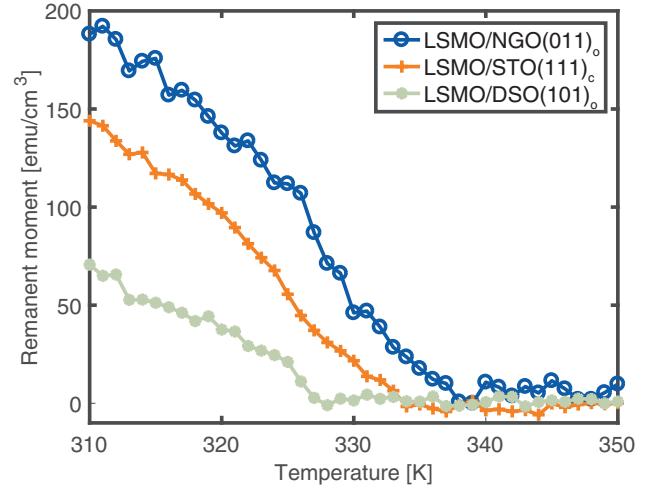
pattern. Both $a^-a^-c^-$ and $a^-a^-c^+$ can result in a hard axis along $[010]_o$ for a certain range of rotation angles. The rotation pattern $a^-a^-c^+$ requires, for a given rotation around a_{pc} and b_{pc}, a larger rotation around c_{pc}, than is the case for the rotation pattern $a^-a^-c^-$. The rotation angle of bulk LSMO is 4.48° [25], while rotations of 6° with a rotation pattern of $a^-a^-a^-$ been found for LSMO on (111)-oriented STO by DFT calculations [35]. LSMO on DSO has a larger average tensile strain then for LSMO on STO. We note that rotations in (111)-oriented LAO are found by DFT to increase close to linear with amount of tensile strain [22], allowing us to extrapolate an expected 10.3° rotational angle for LSMO on DSO. In (001)-oriented thin films, the effective rotations are larger around the most tensile strained direction [36]. Assuming this is also true for (111)-oriented LSMO, the rotations should be largest around the a_{pc} and b_{pc} directions ($a_{pc} = b_{pc} = 3.96$ whilst $c_{pc} = 3.89$). However, from the single ion model calculations, (shown in figure 6) we note that both for $a^-a^-c^+$ and $a^-a^-c^-$ the rotation around c_{pc} is expected to be largest. For a 10.3° rotational angle around a_{pc} and b_{pc}, a minimum of $c_{pc} = 13°$ and $c_{pc} = 10.7°$ is needed to establish the observed anisotropy for $a^-a^-c^+$ and $a^-a^-c^-$ respectively. For the triclinic structure of LSMO on NGO the results from the single ion model calculation in figure 6 indicates that the observed anisotropy is energetically favorable for a range of rotations including no octahedral rotations. DFT studies of (111)-strain indicate that compressive strain results in smaller than bulk rotations around the pseudo-cubic axes [36], consistent with the phase diagram in figure 6.

The remanent magnetization close to the Curie temperature (T_C) for strained LSMO is shown in figure 7. The data were taken while increasing the temperature. The Curie temperature is determined by taking the lowest temperature at which the remanent magnetization vanishes, a method that provides a reliable measure of T_C, though often lower values than when the saturation magnetization is used [37]. The Curie temperatures are found at 328 K, 334 K, and 338 K for the films on

GSO, STO and NGO, respectively. Millis, Darling [38] has proposed a model to describe the effects of strain on the Curie temperature of manganites.

$$T_{\mathrm{C}}(\varepsilon_B, \varepsilon^*) = T_{\mathrm{C}}(0,0)\left[1 - \alpha\varepsilon_B - b\varepsilon^{*2}\right].$$

With $\varepsilon_B = 1/2(2\varepsilon_{111_{\mathrm{pc}}} + \varepsilon_{1-10_{\mathrm{pc}}} + \varepsilon_{11-2_{\mathrm{pc}}})$, a measure of the bulk compression and $\varepsilon^* = 1/4(2\varepsilon_{111_{\mathrm{pc}}} - \varepsilon_{1-10_{\mathrm{pc}}} - \varepsilon_{11-2_{\mathrm{pc}}})$, a measure of the biaxial distortion. An increase in compressive strain and therefore an increased ε_B tends to increase the electron hopping probability, decreasing the effect of the electron lattice coupling and therefore the Curie temperature. The biaxial distortion, ε^*, is related to the Jahn–Teller splitting of the e_g and t_{2g} electron levels. A deviation from $\varepsilon^* = 0$ will increase the localization of the electrons and therefore lower the Curie temperature. Corresponding to ε_B and ε^* are the experimental quantities $\alpha = \frac{1}{T_C}\left[\frac{\mathrm{d}T_C}{\mathrm{d}\varepsilon_B}\right]$ and $b = \frac{1}{T_C}\left[\frac{\mathrm{d}^2 T_C}{\mathrm{d}\varepsilon^{*2}}\right]$, predicted to be approximately 6 and 1400, respectively, for $La_{1.83}Sr_{0.17}MnO_3$ [38]. For $(0\,0\,1)$-oriented LSMO, there are several reports of the values of $T_C(0,0)$, α, and b. Adamo [30] found $T_C(0,0) = 345$ K, $\alpha = 1.55$, $b = 1460$, Tsui [2] reported $T_C(0,0)$, α, and b values of 334 K, 2, and 187, respectively, Angeloni [39] found $b \approx 1000$, and Ranno [40] reported a b value of 1400. From the measured Curie temperatures we find $T_C(0,0) = 333$ K, $\alpha = 3.9$, and $b = -125$. The values of $T_C(0,0)$ and α obtained for LSMO from our set of strain data are in good agreement with the predictions and reported values for $(0\,0\,1)_{\mathrm{pc}}$-oriented films, while b is an order of magnitude lower than most values obtained from $(0\,0\,1)_{\mathrm{pc}}$-oriented films and have opposite sign. From the results of Adamo [30], both the LSMO film on NGO and the LSMO film on DSO are predicted to have a lower T_C than the LSMO film on STO due to the biaxial strain from the orthorhombic substrates. However, here the Curie temperature of the LSMO film on NGO is larger than for LSMO on STO, suggesting that T_C in $(1\,1\,1)_{\mathrm{pc}}$-oriented LSMO thin films is to a smaller degree affected by biaxial strain. This can possibly indicate a smaller degree of Jahn–Teller splitting of the e_g energy levels when applying strain to $(1\,1\,1)_{\mathrm{pc}}$-oriented LSMO films, consistent with that the e_g energy levels do not split due to $(1\,1\,1)_{\mathrm{pc}}$-oriented strain contrary to what is found for $(0\,0\,1)_{\mathrm{pc}}$-oriented strain [41].

Conclusions

In conclusion, $(1\,1\,1)_{\mathrm{pc}}$-oriented LSMO thin films have been grown on NGO, STO, and DSO substrates in order to investigate the effects of strain on structural and magnetic properties. Compressively strained films on NGO are found to be triclinic or monoclinic, while films with tensile strain are found to be rhombohedral on STO and monoclinic on DSO, different from that obtained by $(0\,0\,1)_{\mathrm{pc}}$-oriented strain. A uniaxial magnetic anisotropy is found for the LSMO films on both NGO and DSO with the hard axes along $[1\,0\,0]_o$ and $[0\,1\,0]_o$, respectively. For LSMO on STO, no macroscopic anisotropy is observed. The anisotropy of the LSMO films on STO and NGO is well described by the Néel model of magnetic anisotropy, while for LSMO on DSO, incorporation of octahedral

rotations through the single ion model is needed to explain the uniaxial anisotropy. Lastly, it was found through looking at the Curie temperatures as a function of strain that $(1\,1\,1)_{\mathrm{pc}}$-oriented biaxial strain has a different effect on the Jahn–Teller splitting of e_g and t_{2g} electron levels than observed in $(0\,0\,1)_{\mathrm{pc}}$-oriented LSMO films.

ORCID iDs

T Tybell ● https://orcid.org/0000-0003-0787-8476

References

[1] Haghiri-Gosnet A M and Renard J P 2003 CMR manganites: physics, thin films and devices *J. Phys. D: Appl. Phys.* **36** R127

[2] Tsui F, Smoak M, Nath T and Eom C 2000 Strain-dependent magnetic phase diagram of epitaxial $La_{0.67}Sr_{0.33}MnO_3$ thin films *Appl. Phys. Lett.* **76** 2421–3

[3] Boschker H, Mathews M, Brinks P, Houwman E, Vailionis A, Koster G, Blank D H A and Rijnders G 2011 Uniaxial contribution to the magnetic anisotropy of $La_{0.67}Sr_{0.33}MnO_3$ thin films induced by orthorhombic crystal structure *J. Magn. Magn. Mater.* **323** 2632–8

[4] Boschker H, Mathews M, Houwman E P, Nishikawa H, Vailionis A, Koster G, Rijnders G and Blank D H A 2009 Strong uniaxial in-plane magnetic anisotropy of $(0\,0\,1)$- and $(0\,1\,1)$-oriented $La_{0.67}Sr_{0.33}MnO_3$ thin films on $NdGaO_3$ substrates *Phys. Revi.* B **79** 214425

[5] Nishikawa H, Houwman E, Boschker H, Mathews M, Blank D H A and Rijnders G 2009 Rotation of the magnetic easy axis in $La_{0.67}Sr_{0.33}MnO_3$ thin film on $NdGaO_3(1\,1\,2)$ *Appl. Phys. Lett.* **94** 042502

[6] Steenbeck K and Hiergeist R 1999 Magnetic anisotropy of ferromagnetic La0.7(Sr, Ca)0.3MnO3 epitaxial films *Appl. Phys. Lett.* **75** 1778–80

[7] Liao Z *et al* 2016 Controlled lateral anisotropy in correlated manganite heterostructures by interface-engineered oxygen octahedral coupling *Nat. Mater.* **15** 425–31

[8] Moon E, Colby R, Wang Q, Karapetrova E, Schlepütz C, Fitzsimmons M and May S J 2014 Spatial control of functional properties via octahedral modulations in complex oxide superlattices *Nat. Commun.* **5** 5710

[9] Park J H, Vescovo E, Kim H J, Kwon C, Ramesh R and Venkatesan T 1998 Direct evidence for a half-metallic ferromagnet *Nature* **392** 794–6

[10] Bowen M, Bibes M, Barthélémy A, Contour J-P, Anane A, Lemaitre Y and Fert A 2003 Nearly total spin polarization in $La_{2/3}Sr_{1/3}MnO_3$ from tunneling experiments *Appl. Phys. Lett.* **82** 233–5

[11] Steenbeck K, Hiergeist R, Revcolevschi A and Pinsard-Gaudart L 1999 Magnetic anisotropy in $La_{0.7}(Sr,Ca)_{0.3}MnO_3$ epitaxial thin films and crystals *MRS Proc.* p 562

[12] Khapikov A, Uspenskaya L, Bdikin I, Mukovskii Y, Karabashev S, Shulyaev D and Arsenov A 2000 Magnetic domains and twin structure of the $La_{0.7}Sr_{0.3}MnO_3$ single crystal *Appl. Phys. Lett.* **77** 2376–8

[13] Konoto M, Kohashi T, Koike K, Arima T, Kaneko Y, Tomioka Y and Tokura Y 2004 Magnetic domain structure of a $La_{0.7}Sr_{0.3}MnO_3$ (0 0 1) surface observed by a spin-polarized scanning electron microscope *Appl. Phys. Lett.* **84** 2361–3

[14] Boschker J E, Monsen Å F, Nord M, Mathieu R, Grepstad J K, Holmestad R, Wahlström E and Tybell T 2013 In-plane structural order of domain engineered $La_{0.7}Sr_{0.3}MnO_3$ thin films *Phil. Mag.* **93** 1549–62

[15] Vailionis A, Boschker H, Siemons W, Houwman E, Blank D, Rijnders G and Koster G 2011 Misfit strain accommodation in epitaxial ABO3 perovskites: lattice rotations and lattice modulations *Phys. Rev.* B **83** 064101

[16] Mathews M, Houwman E P, Boschker H, Rijnders G and Blank D H A 2010 Magnetization reversal mechanism in $La_{0.67}Sr_{0.33}MnO_3$ thin films on NdGaO₃ substrates *J. Appl. Phys.* **107** 013904

[17] Chopdekar R V, Arenholz E and Suzuki Y 2009 Orientation and thickness dependence of magnetization at the interfaces of highly spin-polarized manganite thin films *Phys. Rev.* B **79** 104417

[18] Phillips L, Yan W, Moya X, Ghidini M, Maccherozzi F, Dhesi S and Mathur N 2015 Control of magnetization-reversal mechanism via uniaxial anisotropy strength in $La_{0.67}Sr_{0.33}MnO_3$ electrodes for spintronic devices *Phys. Rev. Appl.* **4** 064004

[19] Kim T H *et al* 2016 Polar metals by geometric design *Nature* **533** 68–72

[20] Gibert M, Zubko P, Scherwitzl R, Íñiguez J and Triscone J-M 2012 Exchange bias in LaNiO₃–LaMnO₃ superlattices *Nat. Mater.* **11** 195–8

[21] Hallsteinsen I *et al* 2016 Concurrent magnetic and structural reconstructions at the interface of (1 1 1)-oriented $La_{0.7}Sr_{0.3}MnO_3$/LaFeO₃ *Phys. Rev.* B **94** 201115

[22] Moreau M, Marthinsen A, Selbach S M and Tybell T 2017 First-principles study of the effect of (1 1 1) strain on octahedral rotations and structural phases of LaAlO3 *Phys. Rev.* B **95** 064109

[23] Hallsteinsen I, Folven E, Olsen F K, Chopdekar R V, Rzchowski M S, Eom C B, Grepstad J K and Tybell T 2015 Crystalline symmetry controlled magnetic switching in epitaxial (1 1 1) $La_{0.7}Sr_{0.3}MnO_3$ thin films *APL Mater.* **3** 062501

[24] Hallsteinsen I, Boschker J, Nord M, Lee S, Rzchowski M, Vullum P, Grepstad J, Holmestad R, Eom C and Tybell T 2013 Surface stability of epitaxial $La_{0.7}Sr_{0.3}MnO_3$ thin films on (1 1 1)-oriented SrTiO3 *J. Appl. Phys.* **113** 183512

[25] Radaelli P G, Iannone G, Marezio M, Hwang H Y, Cheong S W, Jorgensen J D and Argyriou D N 1997 Structural effects on the magnetic and transport properties of perovskite $A_{1−x}A'_xMnO_3$ ($x = 0.25, 0.30$) *Phys. Rev.* B **56** 8265–76

[26] Geller S, Curlander P J and Ruse G F 1974 Perovskite-like rare earth gallium oxides prepared at atmospheric pressure *Mater. Res. Bull.* **9** 637–44

[27] Pies W and Weiss A 1976 *e74, XVI. 1.2 Hydroxo-Compounds of Scandium (Hydroxoscandates), XVI. 2 Oxo-Compounds of Yttrium (Oxoyttrates Key Elements: d9-, d10-, d1_d3-, f-Elements* (Berlin: Springer) p 13

[28] Chiarotti G 1995 *1.6 Crystal Structures and Bulk Lattice Parameters of Materials Quoted in the Volume (Structure)* (Berlin: Springer) pp 21–6

[29] Nye J F 1985 *Physical Properties of Crystals: Their Representation by Tensors and Matrices* (Oxford: Oxford University Press)

[30] Adamo C, Ke X, Wang H, Xin H, Heeg T, Hawley M, Zander W, Schubert J, Schiffer P and Muller D 2009 Effect of biaxial strain on the electrical and magnetic properties of (0 0 1) $La_{0.7}Sr_{0.3}MnO_3$ thin films *Appl. Phys. Lett.* **95** 112504

[31] Néel L 1954 Anisotropie magnétique superficielle et surstructures d'orientation *J. Phys. Radium* **15** 225–39

[32] Boschker J A 2011 Perovskite Oxide Heteroepitaxy: Strain and Interface Engineering *Thesis* University of Twente, Zutphen

[33] Skomski R 2008 *Simple Models of Magnetism* (Oxford: Oxford University Press)

[34] Howard C J and Stokes H T 1998 Group-theoretical analysis of octahedral tilting in perovskites *Acta Crystallogr.* B **54** 782–9

[35] Moreau M, Selbach S M and Tybell T 2017 Octahedral coupling in (1 1 1)-and (0 0 1)-oriented $La_{2/3}Sr_{1/3}MnO_3$/ SrTiO₃ heterostructures (arXiv:1710:10996)

[36] Moreau M, Marthinsen A, Selbach S M and Tybell T 2017 Strain-phonon coupling in (1 1 1)-oriented perovskite oxides *Phys. Rev.* B **96** 094109

[37] Boschker H, Verbeeck J, Egoavil R, Bals S, van Tendeloo G, Huijben M, Houwman E P, Koster G, Blank D H A and Rijnders G 2012 Preventing the reconstruction of the polar discontinuity at oxide heterointerfaces *Adv. Funct. Mater.* **22** 2235–40

[38] Millis A J, Darling T and Migliori A 1998 Quantifying strain dependence in 'colossal' magnetoresistance manganites *J. Appl. Phys.* **83** 1588–91

[39] Angeloni M, Balestrino G, Boggio N, Medaglia P, Orgiani P and Tebano A 2004 Suppression of the metal-insulator transition temperature in thin $La_{0.7}Sr_{0.3}MnO_3$ films *J. Appl. Phys.* **96** 6387–92

[40] Ranno L, Llobet A, Tiron R and Favre-Nicolin E 2002 Strain-induced magnetic anisotropy in epitaxial manganite films *Appl. Surf. Sci.* **188** 170–5

[41] Khomskii D I 2014 *Transition Metal Compounds* (Cambridge: Cambridge University Press)